

Study of Penetration Depth and Noise in Microwave Tomography Technique

Abas Sabouni¹ and Sima Noghianian²

¹Department of Biomedical Engineering,
Ecole Polytechnique de Montreal, Montreal, Quebec, H3T1J4, Canada
abas.sabouni@polymtl.ca

²Department of Electrical Engineering, Collage of Engineering and Mines,
University of North Dakota, Grand Forks, North Dakota, 58203, USA
sima.noghianian@enr.und.edu

Abstract — The robustness of the microwave tomography method based on frequency dependent finite difference time domain numerical method and hybrid genetic algorithm for breast cancer imaging for different levels of noise are investigated in this paper. These results indicate the algorithm performs well in the case of data contaminated by various levels of additive white Gaussian noise (up to 15 % of signal strength). Noise levels above this value inhibit the efficacy of the method.

Index Terms — Breast cancer imaging, heterogeneous and dispersive breast tissue, inverse scattering problem, microwave tomography, and penetration depth for different breast types.

I. INTRODUCTION

Microwave tomography (MWT) is the process of creating an image based on dielectric properties' map from measured electric field qualities. The dielectric properties and measured field are related by a non-linear relationship that is modeled by Maxwell's equations. Inverse scattering problem, is the process to determine the physical quantities of the media from the knowledge of the electric field at a set of receiver points outside the scatterer, and knowledge of the source. Applications include non-destructive testing and medical imaging. In spite of the efforts and research in the field of inverse scattering problem, still many important analytical and computational challenges have remained

untouched. Therefore, further efforts are necessary to allow their massive employment in real applications. From a computational point of view, the heterogeneous and dispersive media cause a high computational load. Most of the existing algorithms are very effective when the object under the test is simple. But for applications with complicated structures (such as biomedical imaging, which has a high degree of heterogeneity and high dielectric properties contrast), they may lead to non-real solutions. To deal with these complicated objects, we chose to make no simplification in the non-linear Maxwell's equations. Recently, the authors developed the numerical simulation method based on frequency dependent finite difference time domain ((FD)²TD) and genetic algorithm (GA) for detecting breast cancer [1]. In this paper, the effectiveness of the proposed MWT approach is assessed by means of a numerical example (for breast cancer application) concerning a realistic cross-section of a phantom exposed to an electromagnetic illumination. In MWT imaging technique, the penetration depth plays an important role. Hence, we first analyze the penetration depth of the microwave signal in the breast tissue using anatomically realistic numerical breast phantoms. Then, the proposed microwave tomography technique is applied to a numerical breast phantom with an inhomogeneous scatterer profile, and the map of dielectric properties inside the breast phantom is reconstructed. The presence of noise in the synthetic data is also considered

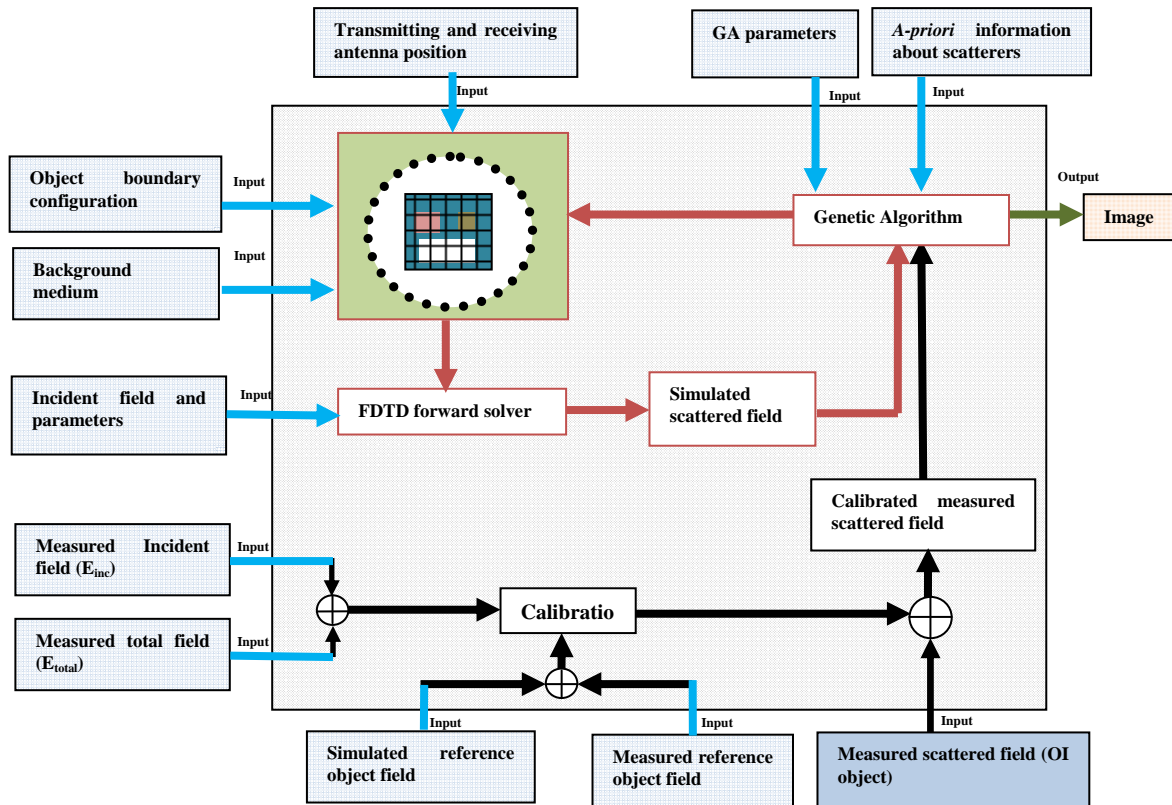


Fig. 1. Block diagram of the proposed MWT method.

and the dependence of the reconstruction accuracy on the signal-to-noise ratio (SNR) is investigated. The paper is organized as follows. In section II, the methodology for the proposed MWT system is explained. In section III we discuss MWT for breast cancer detection and penetration depth for different types of breast phantom is calculated. Section IV discusses the inversion results for the synthetic data and in section V we discuss the inversion results where noise is present.

II. METHODOLOGY

Figure 1 shows the block diagram of the proposed MWT method in [1]. The proposed MWT technique requires a priori information about object of interest (OI), imaging domain, background medium, and measured scattered field from an OI as well as a reference object. As can be seen in this figure, the quality of the images depends on the accuracy of a priori information, accuracy in measured fields, and forward and inverse algorithms. A priori information include information about scatterer, background medium, positions of the transmitter and receiver antennas,

and scattered field of a known object for calibration purpose.

III. MICROWAVE IMAGING FOR BREAST CANCER DETECTION

In recent years, microwave imaging has attracted significant interest for biomedical applications in general and as an alternative or complementary method to X-ray mammography for breast imaging in particular. This method relies on the contrast between the electrical properties of tumor and those of normal tissue. Microwave breast imaging techniques can be divided into three main categories: passive [2], hybrid [3], and active methods [1]. In active imaging approaches, the patient lies in the prone position and the transmitter and receiver antennas are located around the breast. A transmitter antenna is fixed at the specific radius from the breast and transmits a signal; the scattered field is collected by receiver antennas around the breast at a specific radius while they are at the same plane of transmitter antenna. This imaging method uses energy at

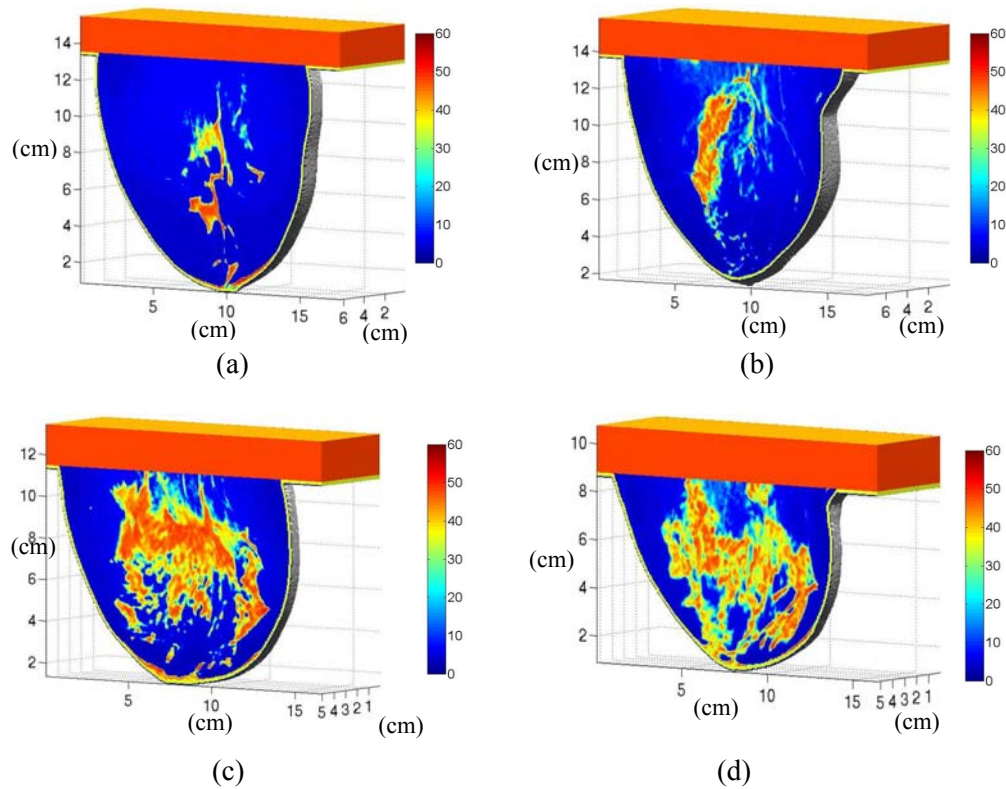


Fig. 2. 3D map of relative permittivity at 5 GHz for (a) mostly fatty, (b) scattered fibro-glandular, (c) heterogeneously dense, and (d) very dense breast type (generated from MRI data in [4]).

microwave frequency range to penetrate into the body and retrieve structural and functional information about the tissues via the scattered waves. Due to the difference between the dielectric properties of the normal and malignant tissues, a scattered electromagnetic field, corresponding to each incident field, will arise which is then measured outside the breast and used to find the shape, location, and dielectric properties of the normal and malignant tissue.

A. Numerical breast phantom

For simulating the breast, in this paper, we used a numerical breast phantom derived from magnetic resonance images (MRI). Figure 2 depicts maps of dielectric properties for the spatial distribution of media numbers for different breast types in terms of X-ray mammography descriptors: mostly fatty, scattered fibro-glandular, heterogeneously dense, and very dense. These were derived from a series of T1-weighted MRIs of the patient in a prone position, provided by the University of Wisconsin-Madison [4]. Figure 2 (a), (b), (c), and (d) show the corresponding

dielectric map. Each phantom contains three variations of both fibro-glandular and a adipose tissues, as well as transitional tissues. Dimensions within the 3D region of the breast are described according to each axis. The z -axis signifies the depth, and the x and y -axes represent the span and breadth of the breast, respectively. In order to create the dielectric properties map from the MRI, the range of MRI pixel densities in the breast interior have been linearly mapped to the range of the percentage of water content and to tissue type, such as skin, muscle, fatty, fibro-glandular, and transitional, for each voxel. Figure 3 shows the cross-sectional view in the x - y plane of tissue types for different breast phantoms in terms of X-ray descriptors. The color bar in this figure indicates the different tissue types; the red color shows the fatty tissue, the orange color shows the transitional tissue, the yellow color shows the fibro-glandular tissue, and the dark blue represents the skin, while the medium blue color represents the immersion medium. Figure 4 shows the cross-sectional view in the x - y plane in terms of water content for four types of breast phantoms. The

color bar illustrates the water content over a pixel, ranging from zero to one. The fatty and fibro-glandular tissues were divided into three different

groups. Therefore, in each group the water content varies independently within a range of values from zero to one.

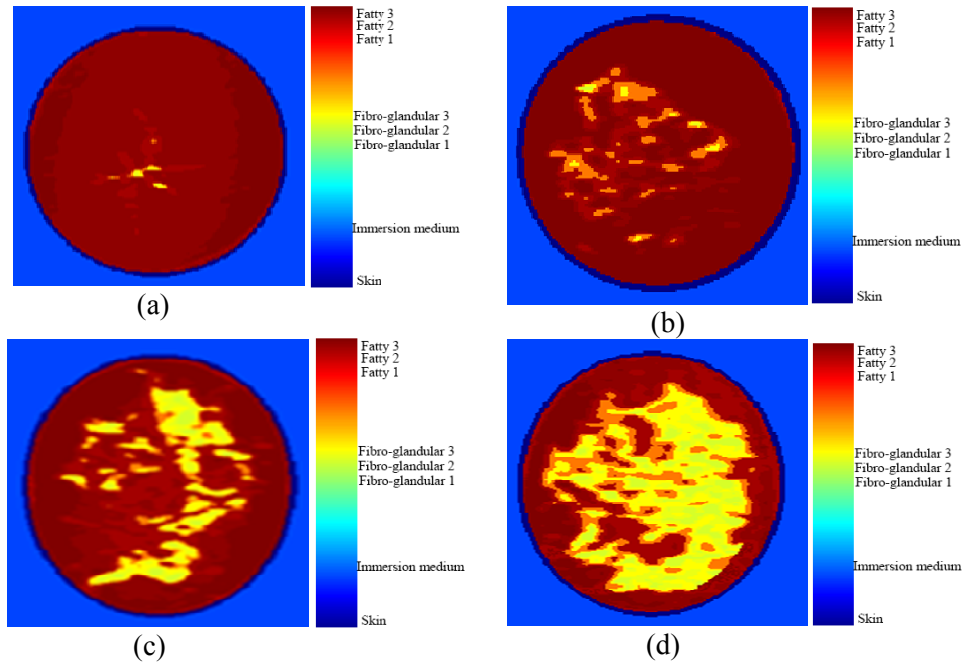


Fig. 3. 2D sectional views of the different breast phantoms in terms of media type (a) mostly fatty, (b) scattered fibro-glandular, (c) heterogeneously dense, and (d) very dense breast type.

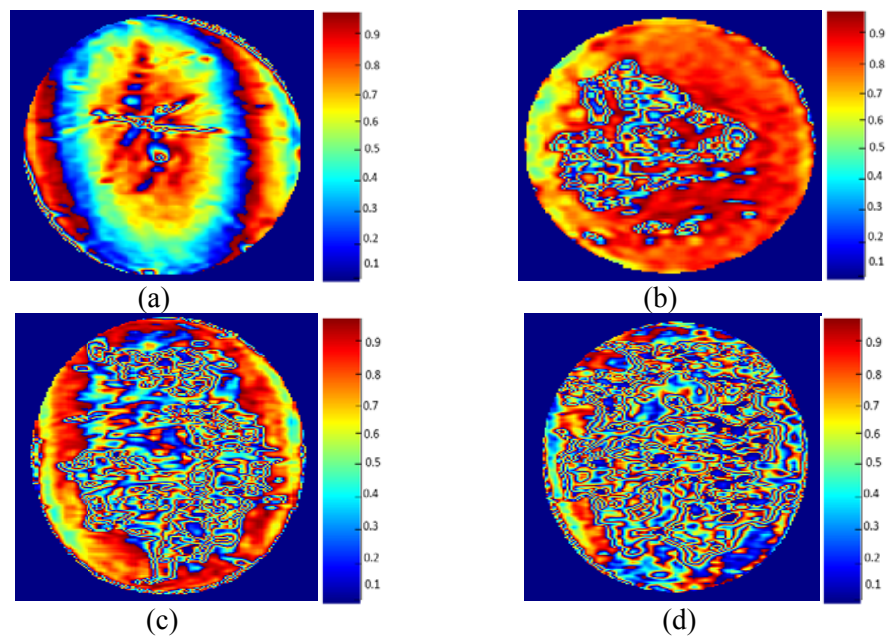
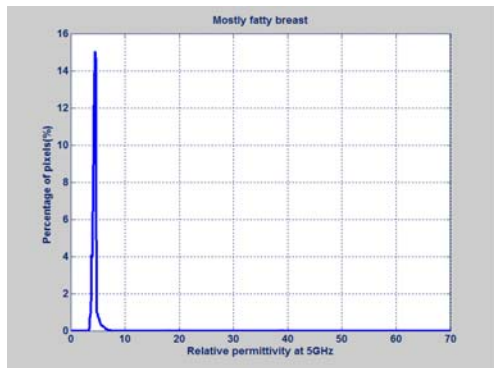


Fig. 4. 2D sectional views of the different breast phantoms in terms of water content (a) mostly fatty, (b) scattered fibro-glandular, (c) heterogeneously dense, and (d) very dense breast type.

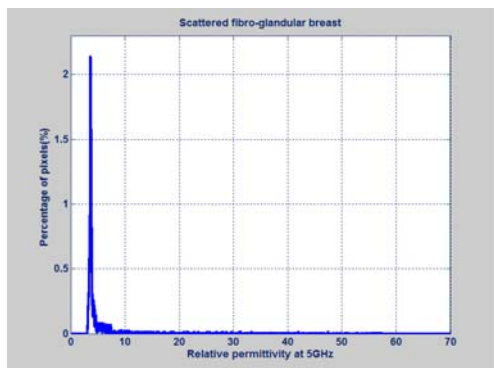
We used these two pieces of information (type and water content), for each voxel and mapped

them to appropriate Debye parameters [5]. In order to show the majority of fatty tissue in all types of

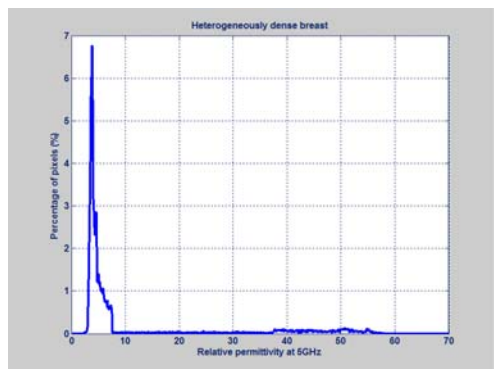
breast phantoms and how the amount of fibro-glandular tissue changes in these four types of breast tissue, we performed a data analysis. In an image of permittivity, each pixel of image has a value of permittivity ranging from 0 to 70. To calculate histograms of permittivity, the total number of pixel that fall into each value of permittivity, divided by the total number of pixels. Figure 5 shows the histogram of the permittivity for different numerical breast phantoms at 5 GHz.



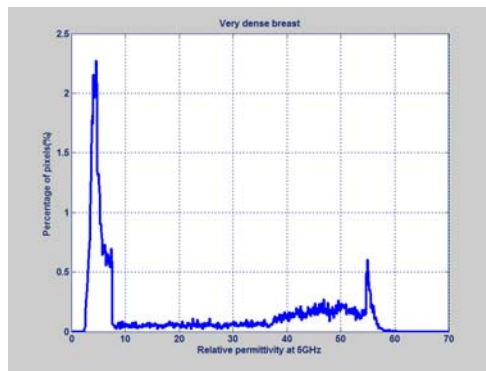
(a)



(b)



(c)



(d)

Fig. 5. The histogram of the permittivity for different numerical breast phantoms at 5 GHz (a) mostly fatty, (b) scattered fibro-glandular, (c) heterogeneously dense, and (d) very dense.

All the analysis is conducted at the cross-section 4 cm away from the nipple. Several observations can be drawn from these graphs. First, as we move from mostly fatty to the very dense breast phantom, the percentage of fatty tissue decreases, and the percentage of fibro-glandular tissue increases. Second, each breast phantom almost covers the entire range of dielectric constants from 0 to 70, and furthermore, the distribution of dielectric constants is not uniform.

B. Penetration depth

The principal limiting factor in penetration depth of the microwave is attenuation of the electromagnetic wave in the breast tissues. The attenuation predominantly results from the conversion of electromagnetic energy to thermal energy due to the high conductivities of the skin and breast tissue at high frequencies. Figure 6 illustrates that the conductivities of the skin, the fibro-glandular tissue, and the malignant tumor increase by increasing the frequency with a constant amount of water. In this section, we focus on the investigation of the penetration depth of the microwave pulse into the numerical breast phantom, and we compare the scattered fields for each case of Fig. 2. The penetration depth is the distance that the propagation wave will travel before the power density is decreased by a factor of $1/e$. The absorbed power density is given by,

$$\text{Absorb power density} = \frac{\sigma_{\text{average}}}{2} |E_{\text{total}}|^2 \quad (1)$$

where σ_{average} is the average of conductivity for breast tissues and E_{total} is the total field. In order to calculate the penetration depth, we used 2D (FD)²TD that includes the water content [5, 6]. The (FD)²TD is an extended version of the conventional finite difference time domain (FDTD) that incorporates the Debye model into the difference equations and can handle dispersive materials more accurately [7]. The breast model is based on an MRI data taken from the breast phantom repository [4] as explained in section III-A. Each cell of the (FD)²TD contains its own tissue type and percentage of water content. For the study of the penetration depth, the breast is surrounded by free space. Figure 7 shows the depth of penetration as a function of frequency for different types of numerical breast phantoms.

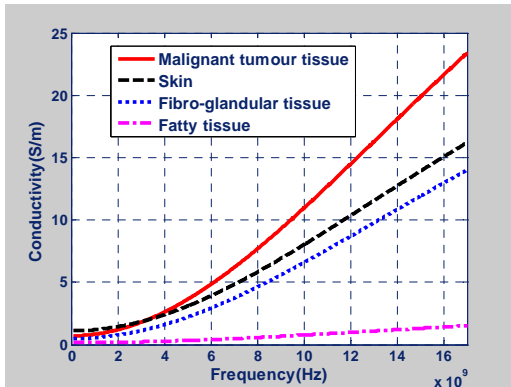


Fig. 6. Frequency variation of conductivity for different breast tissues with 50 percent water content based on Debye model.

As can be seen in this graph, the $1/e$ depth of penetration is different for each case. This is due to different tissue compositions in different types of numerical breast phantoms. The penetration depth inside the dispersive lossy biological media decreases as the frequency increases. Therefore, employing higher frequencies to obtain better resolutions and improved imaging accuracy remains a challenge.

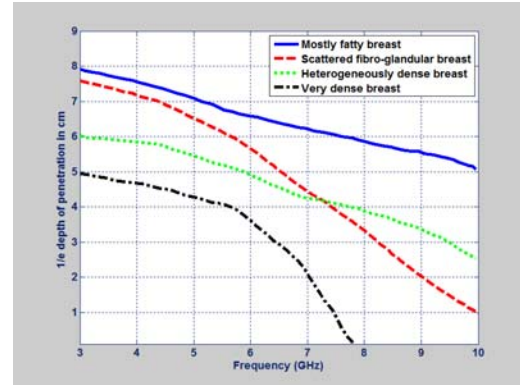
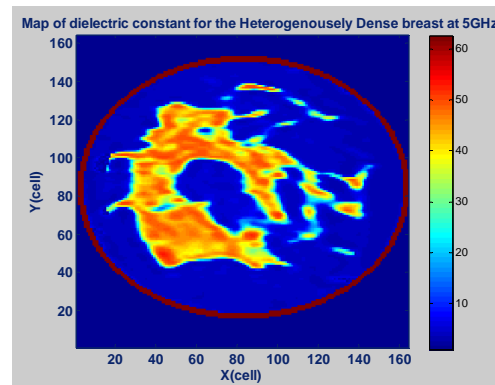


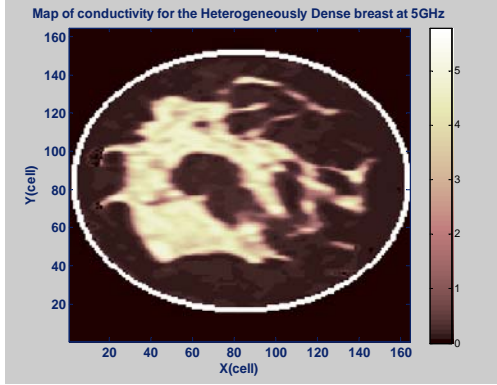
Fig. 7. The $1/e$ penetration depth versus frequency for different breast phantoms.

IV. INVERSION RESULTS FOR BREAST CANCER DETECTION

In order to show the ability of the proposed method in terms of resolution, the breast phantom derived from MRI [4] data with a 7 mm resolution has been selected. Cross-sectional maps of the dielectric constant and effective conductivity distribution at 5 GHz for a “heterogeneously dense” breast phantom are shown in Fig. 8. The physical diameter of the breast phantom is approximately 8 cm. The phantom contains different tissue types ranging from the highest water content (fibro-glandular) tissue to lowest water content (fatty) tissue, and also a transitional region with various water content levels.



(a)



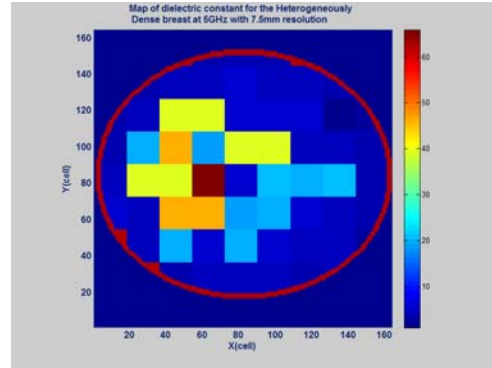
(b)

Fig. 8. Map of (a) permittivity and (b) conductivity of the heterogeneously dense breast phantom.

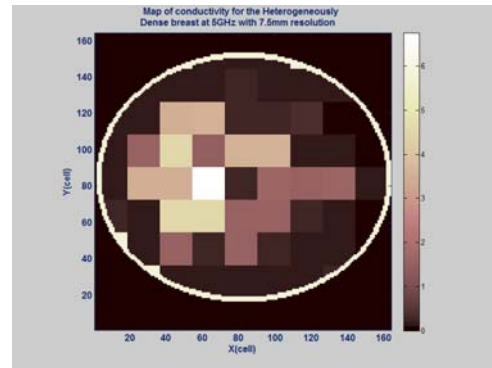
Figure 9 shows the map of the dielectric properties at 7 mm resolution of the numerical breast phantom shown in Fig. 8. A 7 mm square-shaped tumor was inserted inside the fibroglandular tissue for the phantom used in the FDTD model. The tumor is placed at a $x = 60$ cm and $y = 80$ cm position. The breast is surrounded by the free space. In the examples considered herein, the following parameters have been used. 100 observation points are uniformly distributed around the investigation domain. A (Transverse Magnetic) TM_z Gaussian plane wave successively illuminates the breast and penetrates in the investigation domain, and the scattered fields are measured at the observation points around it. To enhance the accuracy of the image and reduce the ill-posedness of the inverse problem, the procedure is repeated for four different incident angles (0° , 90° , 180° , and 270°). In these examples the measurement data is replaced by hypothetical simulated data obtained by running a forward simulation using $(FD)^2TD$ with a 0.1 mm resolution. To prevent the inverse crime, a 0.5 mm resolution mesh has been used for the inverse solver. Equation 2 shows the fitness-function used in the GA optimization,

$$\text{Fitness} = 1 - \frac{1}{T} \sum_{i=1}^T \left\| \sum_{f=f_1}^{f_2} \sum_{\Phi=1}^M \frac{(E_{\Phi,i,f}^{\text{measurement}} - E_{\Phi,i,f}^{\text{simulation}})^2}{(E_{\Phi,i,f}^{\text{measurement}})^2} \right\| \quad (2)$$

The $E_{\Phi,i,f}^{\text{measurement}}$ is the measured scattered electric field, $E_{\Phi,i,f}^{\text{simulation}}$ is the estimated scattered field obtained by performing a forward simulation, M is the number of observation points, T is the total number of illumination angles, and ϕ is an index to angle of the observation point from the axis of the incident wave. f refers to different sampling frequencies within f_1 and f_2 .



(a)



(b)

Fig. 9. Map of the (a) permittivity and (b) conductivity of the heterogeneously dense breast with 7 mm resolution.

Note that the data at each frequency are equally weighted in the inversion process. As a proof of concept, we have considered the noiseless scenario for the first example and in the second example the effect of the noise in inversion results is investigated.

A. Optimization procedure

In the GA program, the enclosed scattering region (inside the breast) is discretized into a number of small patches ($7 \times 7 \text{mm}^2$). We assumed

that the location of the skin is known and can be found using skin detection technique [8]. Then the GA optimization starts from a homogeneous fatty tissue background and fills in some patches of possible materials inside the area and try to find a set of dielectric properties of the material for those patches that can generate the same scattered fields as the hypothetical simulated data.

The reconstruction algorithm consists of a combination of a binary and areal GA [9]. The GA optimization is divided into two steps. At the first step, the binary genetic algorithm (BGA) is employed in order to determine the type of the tissue for each patch. In the second step, by using real genetic algorithm (RGA) for the candidate solutions the search is performed for the right amount of water content. In the BGA, the look-up table consists of first order Debye parameters for four different tissue types: fibro-glandular, fatty, transitional, and malignant tissues with 50 percent water content given in Table 1 [10, 11].

Table 1: Look-up table of the Debye parameters for the BGA.

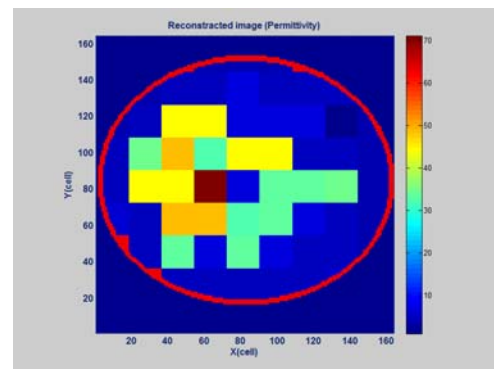
| Medium | Fat | Transitional | Fibro-glandular | Malignant Tumour |
|---------------------|------|--------------|-----------------|------------------|
| ϵ_{∞} | 4.33 | 22.46 | 52.020 | 76.170 |
| ϵ_s | 2.98 | 8.488 | 14.000 | 25.520 |
| $\sigma_s(S/m)$ | 0.02 | 0.230 | 0.780 | 1.200 |
| $\tau_0(ps)$ | 13.0 | 13.00 | 13.00 | 13.00 |

For each patch, a two bit identifier can designate it as one of four types of tissue. In BGA the chromosome is expressed as a binary string. Therefore, the search space of the considered problem is mapped into a binary space. After reproducing an offspring, a decoder mapping is applied to the look up table to map them back to real space in order to compute their fitness-function values. The optimizing parameter here is the type of breast tissue for each patch of search space. The BGA program stops when the average quality of the population does not improve after a number of generations. The best individuals of the last generation of BGA are passed to the second step, which is RGA. For the RGA, the look-up table consists of first order Debye parameters from the upper to lower end of the range for four the same types of breast tissue with various water content levels (Table 2) [10, 11].

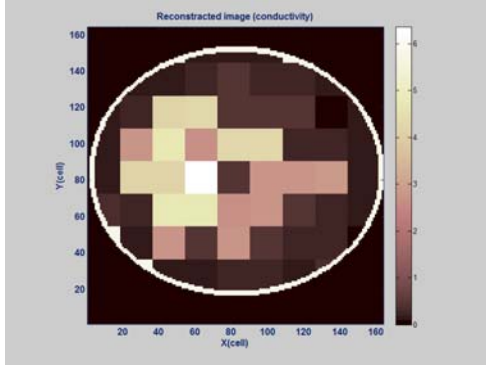
Table 2: Look-up table of the Debye parameters for the RGA.

| Medium | Fat | Transitional | Fibro-glandular | Malignant Tumour |
|-----------------------|-------|--------------|-----------------|------------------|
| $\epsilon_{\infty u}$ | 3.987 | 12.990 | 23.200 | 9.058 |
| ϵ_{su} | 7.535 | 37.190 | 69.250 | 60.360 |
| $\sigma_{su}(S/m)$ | 0.080 | 0.397 | 1.306 | 0.899 |
| $\epsilon_{\infty l}$ | 2.309 | 3.987 | 12.990 | 23.200 |
| ϵ_{sl} | 2.401 | 7.535 | 37.190 | 69.250 |
| $\sigma_{sl}(S/m)$ | 0.005 | 0.080 | 0.397 | 1.306 |
| $\tau_0(ps)$ | 13.00 | 13.00 | 13.00 | 13.00 |

RGA optimizes the percentage of water content. Including the percentage of water content into the Debye model has been discussed in reference [5]. The result of BGA is a map of the dielectric properties inside the breast phantom (assuming 50 % water content) and for the RGA is the water content of that tissue. It is worth mentioning that the GA programs are not guaranteed to converge to the optimal solution, but by using RGA and looking at the behavior of the best fitness values at different generations for each individual of those possible solutions obtained by BGA, one can choose a population that is adequate to the problem and thus increase the chance of success. Figure 10 shows the reconstructed image of permittivity and conductivity. Transects of the reconstructed permittivity and conductivity at 5 GHz in the horizontal direction at line $y = 80$ cell and $x = 64$ cell, compared with the actual distribution, are shown in Fig. 11.

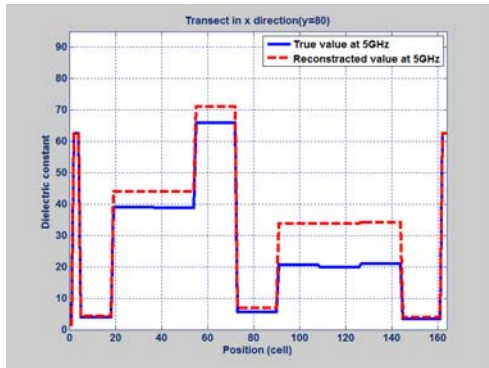


(a)

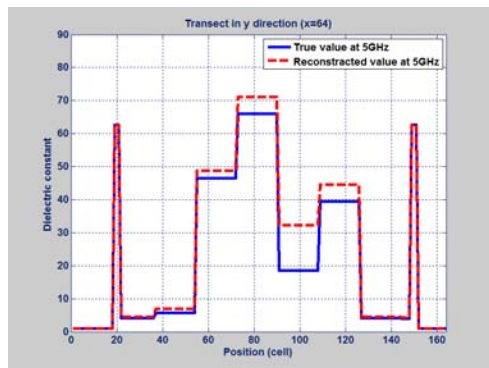


(b)

Fig. 10. Reconstructed image of (a) permittivity, and (b) conductivity for the breast phantom of Fig. 9.



(a)



(b)

Fig. 11. Transects of the reconstructed permittivity image at (a) $y = 80$ cell horizontal direction and (b) $x = 64$ cell vertical direction profiles compared with the actual distribution.

One observation apparent in these images is the small degree of inaccuracy in the recovered

permittivity and conductivity compared with the actual profile, since the percentage of water content, which affects dielectric properties, is not precisely known. However, the estimated percentage of water content is within the range for each tissue type to recognize the right tissue composition.

V. HGA/FDTD IN THE PRESENCE OF NOISE

Background noise is always present in any measurement and it must be taken into account. This is particularly important in biomedical applications, since for safety reasons, it is not possible to increase the energy of the incident field to overshadow the background noise. It is shown in this section that the proposed method is efficient and provides adequate accuracy even when the signal to noise ratio (SNR) is low. SNR is defined by [12]

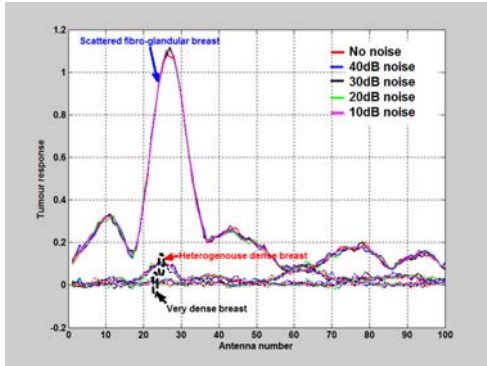
$$SNR = 10 \log \left(\frac{P_s}{P_n} \right), \quad (3)$$

in which P_s is the total power of the scattered field and is proportional to

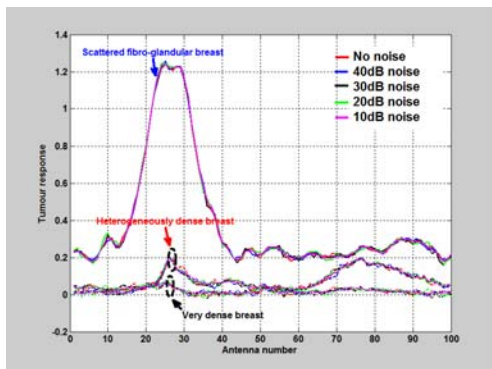
$$P_s = \frac{1}{2} \sum_{f_1}^{f_2} |E_z|^2. \quad (4)$$

The symbol E_z is the scattered field at the different frequencies within $f_1 - f_2$ range, and P_n is the noise power. Figure 12 shows the tumor response for 1 cm tumor (Fig. 12 (a)) and 5 mm tumor (Fig. 12 (b)) while the data is contaminated with different levels of noise (SNR = 10, 20, 30, and 40 dB) for different types of breasts such as scattered fibro-glandular breast, heterogeneously dense breast, and very dense breast at 5 GHz. As can be seen in this figure the strength of tumor response for the scattered fibro-glandular breast is quite high compared to the heterogeneously dense breast and very dense breast. Because, the amount of the fibro-glandular tissue (which is a lossy material) in heterogeneously dense breast and very dense breast is significantly large. We artificially added some noise to the signal to mimic the existing noise in measurement setup. Figure 12 shows that for the scattered fibro-glandular breast by adding different level of noise the signal intensity is still well above the noise floor. However, for the very dense breast, due to small signal strength, it will

be difficult to distinguish between the signal and noise. We did not provide the results of mostly fatty breast here. Generally the tumor response for this type is stronger than all other breast.



(a)



(b)

Fig. 12. Tumor response for diverse SNR and different breast types and tumor size with diameter (a) 1 cm and (b) 5 mm.

The 2 mm tumor response without noise for the heterogeneously dense breast and very dense breast are compared with the response of 1 cm and 5 mm tumors and are shown in Fig. 13. Table 3 also shows the maximum tumor response for the heterogeneously dense breast and very dense breast. As can be seen, the tumor response for the 2 mm tumor in heterogeneously dense breast is even higher than the response from 1 cm tumor in very dense breast.

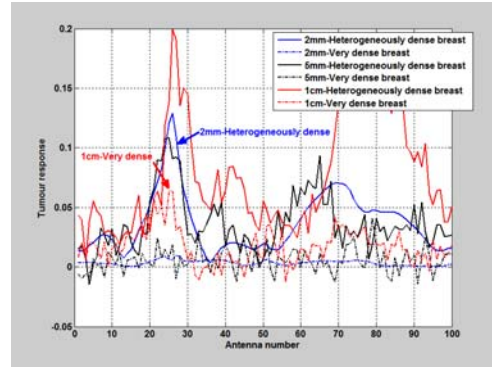


Fig. 13. Tumor response for 1 cm, 5 mm and, 2 mm diameter tumor sizes for the heterogeneously dense breast and very dense breast.

Table 3: Maximum tumor response.

| Tumour size | 1cm | 5mm | 2mm |
|------------------------------|-------|-------|-------|
| Heterogeneously dense breast | 0.199 | 0.108 | 0.128 |
| Very dense breast | 0.063 | 0.041 | 0.009 |

Therefore, detecting the small tumor becomes difficult as the amount of the fibro-glandular tissue increases in the breast. Therefore, the detectable tumor size depends on the breast type and SNR. Here, we investigated the performance of the proposed method at different SNR levels. Figure 14 shows the block diagram of the process of adding the noise to the measurement signal.

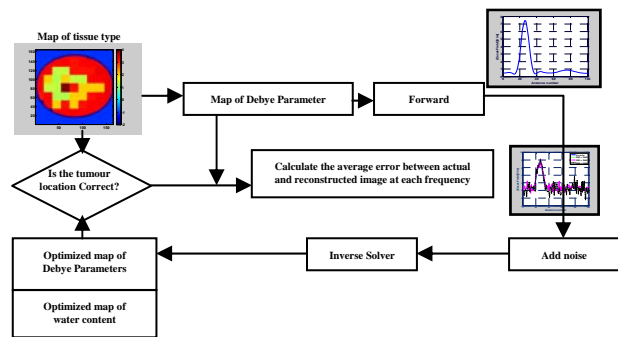
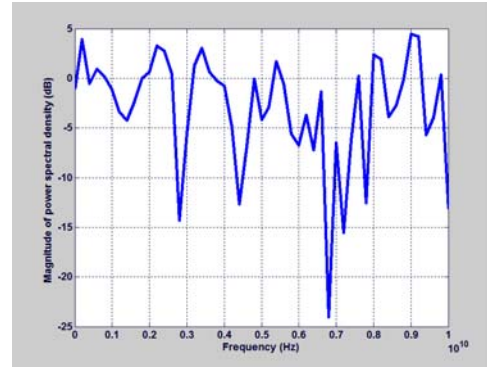


Fig. 14. Block diagram of adding noise in the proposed tomography method.

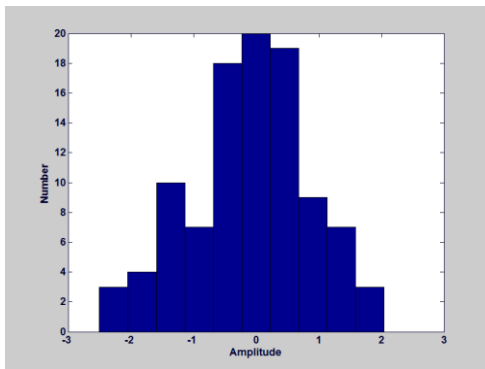
After recording the scattered fields at the observation points by using the $(FD)^2TD$ solver, an additive white Gaussian noise was added to

simulate the instrument noise, which can present in real measurements. The HGA optimization technique was then used to reconstruct the dielectric property map of the breast tissue inside the numerical breast phantom. Background noise generally considered as white noise, due to having an almost a constant power spectral density [12]. Figure 15 (a) shows the histogram of white noise. Figure 15 (b) shows the amplitude of white noise for each antenna at the observation point at 5 GHz. Figure 15 (c) presents the power spectral density of the white Gaussian noise for each antenna. The white noise was artificially added to all measurements of the scattered field at different frequencies in such a way that the power of noise was constant at all frequencies, but the power of the noise changed randomly with Gaussian distribution at each observation point.

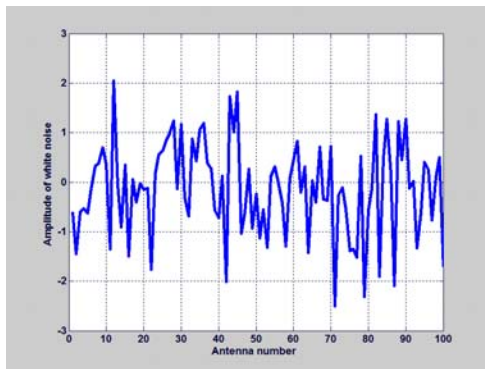


(c)

Fig. 15. (a) Histogram plot of the added white noise, (b) amplitude of white noise for each antenna at the observation point, and (c) power spectral density of the white Gaussian noise.



(a)



(b)

To illustrate the ability and robustness of the proposed HGA method, we added different levels of noise to the scattered field of the breast phantom of Fig. 9 by using the process shown in Fig. 14. Figures 16 (a) and (b) show the average error of the dielectric constant and conductivity versus SNR, respectively. These errors are averaged over the differences between the actual and the reconstructed permittivity and conductivity shown in equations (5) and (6), respectively,

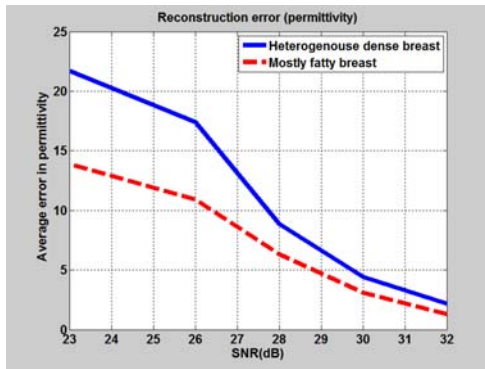
Average error in permittivity =

$$= \sum_{f_1}^{f_2} \frac{\sum_i \sum_j |\epsilon_{r(reconstructed\ image)} - \epsilon_{r(real\ image)}|}{\text{number of cells}} \quad (5)$$

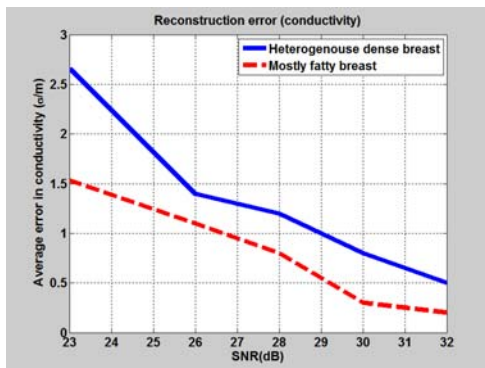
Average error in conductivity =

$$= \sum_{f_1}^{f_2} \frac{\sum_i \sum_j |\sigma_{(reconstructed\ image)} - \sigma_{(real\ image)}|}{\text{number of cells}}, \quad (6)$$

where f_1 and f_2 refer to different frequencies of reconstruction and i and j are the cell numbers in the x and y directions, respectively. These figures demonstrate that as the SNR decreases (noise level increases), the average error increases. It was observed that the proposed method still can find the tissue types of the heterogeneous structure even when the SNR is 23 dB, which is equivalent to 15 % background noise. When the background noise is greater than 15 %, the optimization program did not converge.



(a)



(b)

Fig. 16. The average error in (a) dielectric constant and (b) conductivity versus SNR.

It was also noticed that by increasing the noise level, the optimization time for convergence was significantly increased. The same procedure of adding noise was repeated for the mostly fatty breast. As indicated in Fig. 16, the average error of permittivity and conductivity are less, compared to heterogeneously dense breast with the same SNR.

VI. CONCLUSION

In this paper we studied the noise effects on $(FD)^2TD/GA$ algorithm for solving the inverse scattering problem for heterogeneous and dispersive objects. We presented an accurate simulation model for the breast cancer detection that considers the heterogeneity, dispersive characteristics, and the water content of the breast. Further, we calculated the penetration depth for different tissue compositions of breast phantoms categorized as: mostly fatty, scattered fibroglandular, heterogeneously dense and very dense.

We have presented the results of inversion and the effect of noise on the accuracy of proposed microwave tomography method. The simulation results illustrate that the proposed method is capable of detecting lesions in environments where they are surrounded by fibro-glandular tissue, which happens in most cases of breast cancer. We used 7 mm resolution for GA. Higher resolution images of the realistic phantom can be obtained by reducing the discretization unit size, which result in a longer run time. In this paper the breast cancer detection is chosen as a primary application to investigate the capabilities of the proposed technique due to the heterogeneous structure and dispersive characteristic of the breast. However, the proposed technique can be applied to many other applications.

ACKNOWLEDGMENT

The authors would like to acknowledge the financial support of Natural Sciences and Engineering Research Council of Canada, Cancer Care Manitoba, University of North Dakota, and North Dakota Experimental Program to Stimulate Competitive Research.

REFERENCES

- [1] A. Sabouni, S. Noghianian, and S. Pistorius, "A global optimization technique for microwave imaging of the inhomogeneous and dispersive breast," *Canadian Journal of Electrical and Computer Engineering*, vol. 35, no.1, pp. 15-24, 2010.
- [2] S. Iudicello and F. Bardati, "Functional imaging of compressed breast by microwave radiometry," *Applied Computational Electromagnetics Society (ACES) Journal*, vol. 24, no. 1, pp. 64-71, 2009.
- [3] G. Zhu and M. Popovic, "Enhancing microwave breast tomography with microwave-induced thermo acoustic imaging," *Applied Computational Electromagnetics Society (ACES) Journal*, vol. 24, no. 6, pp. 618-627, 2009.
- [4] E. Zastrow, S. K. Davis, M. Lazebnik, F. Kelcz, B. D. Van Veen, and S. C. Hagness, "Database of 3D grid-based numerical breast phantoms for use in computational electromagnetics simulations," *Instruction Manual*, University of Wisconsin-Madison.
- [5] A. Sabouni, S. Noghianian, and S. Pistorius, "Water content and tissue composition effects on microwave tomography results," in *International Review of Progress in Applied Computational Electromagnetics (ACES)*, 2008.

- [6] A. Sabouni, S. Noghianian, and S. Pistorius, "Frequency dispersion effects on FDTD model for breast tumor imaging application," in *IEEE Antennas and Propagation Society International Symposium*, pp. 1410-1413, 2006.
- [7] M. Bui, S. Stuchly, and G. Costache, "Propagation of transients in dispersive dielectric media," *IEEE Transactions on Microwave Theory and Techniques*, vol. 39, no. 7, pp. 1165-1172, 1991.
- [8] D. A. Woten and M. El-Shenawee, "Quantitative analysis of breast skin for tumor detection using electromagnetic waves," *Applied Computational Electromagnetics Society (ACES) Journal*, vol. 24, no. 5, pp. 458-463, 2009.
- [9] A. Sabouni, A. Ashtari, S. Noghianian, G. Thomas, and S. Pistorius, "Hybrid binary-real GA for microwave breast tomography," in *Antennas and Propagation Society International Symposium*, pp. 1-4, July 2008.
- [10] M. Lazebnik, L. McCartney, D. Popovic, B. Watkins, M. J. Lindstrom, J. Harter, S. Sewall, A. Magliocco, J. H. Booske, M. Okoniewski, and S. C. Hagness, "Large-scale study of the ultra-wideband microwave dielectric properties of normal breast tissue obtained from reduction surgeries," *Physics in Medicine and Biology*, vol. 52, pp. 2637-2656, 2007.
- [11] M. Lazebnik, D. Popovic, L. McCartney, C. Watkins, M. Lindstrom, J. Harter, S. Sewall, T. Ogilvie, A. Magliocco, T. M. Breslin, W. Temple, D. Mew, J. H. Booske, M. Okoniewski, and S. C. Hagness, "A large-scale study of the ultra-wideband microwave dielectric properties of normal, benign, and malignant breast tissues obtained from cancer surgeries," *Physics in Medicine and Biology*, vol. 52, pp. 6093-6115, 2007.
- [12] M. Moghaddam and W. Chew, "Study of some practical issues in inversion with the born iterative method using time-domain data," *IEEE Transactions on Antennas and Propagation*, vol. 41, no. 2, pp. 177-184, 1993.



Abas Sabouni received the M.Sc. degree in Electrical Engineering from K. N. Toosi University, Tehran, Iran, in 2005, and Ph.D. degree in Electrical Engineering, from the University of Manitoba, Winnipeg, MB, Canada, in 2011. Since 2010, he has been a Post-Doctoral Fellow in Biomedical Engineering Department at the Ecole Polytechnique de Montreal,

and Research Associate at the Department of Electrical and Computer Engineering at the Concordia University from 2011. He was a Research and Development Engineer at PartoDadeh Inc., Tehran, Iran during 2001 through 2004. During 2005 and 2006, he was a Research Assistant in the Electromagnetic Group, University of Manitoba and a Research Associate at Cancer Care Manitoba. From 2009 to 2010, he was a Research Associate in the Department of Electrical Engineering, University of North Dakota, Grand Forks, North Dakota, USA. His research interests include inverse scattering problem, microwave imaging, UWB antenna design and modeling, and transcranial magnetic stimulation. Dr. Sabouni is the recipient of the IEEE AP-S Honorable Mention Student Paper Contest 2008. In 2013, he served as the Vice-President of IEEE Montreal section. Since 2010, he is the Chair of IEEE Montreal Antenna Propagation Chapter.



Sima Noghianian received the B.Sc. degree in Electrical Engineering from the Sharif University of Technology, Tehran, Iran, in 1992, and the M.Sc. and Ph.D. degrees, both in Electrical Engineering, from the University of Manitoba, Winnipeg, Canada, in 1996 and 2001, respectively. In 2001, she was at Yotta Yotta Corporation, Edmonton, Canada. She was an Assistant Professor in the Department of Electrical Engineering, Sharif University of Technology during 2002 and 2003. From 2003 to 2008, she was an Assistant Professor in the Department of Electrical and Computer Engineering, University of Manitoba. Since 2008, she has been an Assistant Professor in the Department of Electrical Engineering, University of North Dakota, Grand Forks. Her research interests include antenna design and modeling, wireless channel modeling, ultra-wideband antennas, and microwave imaging. Dr. Noghianian was IEEE Winnipeg Waves (joint Chapter of Antenna and Propagation/Microwave Theory and Techniques/Vehicular Technology societies) Chapter Chair during 2004 and 2005. She received a Postdoctoral Fellowship from Natural Sciences and Engineering Research Council of Canada at the University of Waterloo in 2002.